Gravitational atmospheric tides as a probe of Titan's interior: Application to Dragonfly

B. Charnay, G. Tobie, S. Lebonnois, R. D. Lorenz

**Astronomy
&
Astrophysics**

Gravitational atmospheric tides as a probe of Titan's interior: Application to Dragonfly

B. Charnay[1], G. Tobie[2], S. Lebonnois[3], and R. D. Lorenz[4]

[1] LESIA, Observatoire de Paris, Université PSL, CNRS, Sorbonne Université, Université de Paris, 5 Place Jules Janssen, 92195 Meudon, France
e-mail: `benjamin.charnay@obspm.fr`
[2] Laboratoire de Planétologie et de Géodynamique, UMR 6112, CNRS, Université de Nantes, 2 rue de la Houssinière, BP 92208, 44322 Nantes cedex 03, France
[3] Laboratoire de Météorologie Dynamique (LMD/IPSL), Sorbonne Université, ENS, PSL Research University, Ecole Polytechnique, Institut Polytechnique de Paris, CNRS, Paris, France
[4] Johns Hopkins Applied Physics Lab, Laurel, MD, USA

ABSTRACT

Context. Saturn's massive gravity is expected to causes a tide in Titan's atmosphere, producing a surface pressure variation through the orbit of Titan and tidal winds in the troposphere. The future Dragonfly mission could analyse this exotic meteorological phenomenon.
Aims. We aim to analyse the effect of Saturn's tides on Titan's atmosphere and interior to determine how pressure measurements by Dragonfly could constrain Titan's interior.
Methods. We model atmospheric tides with analytical calculations and with a 3D global climate model (the IPSL-Titan GCM), including the tidal response of the interior.
Results. We predict that the Love numbers of Titan's interior should verify $1 + \Re(k_2 - h_2) \sim 0.02$–$0.1$ and $\Im(k_2 - h_2) < 0.04$. The deformation of Titan's interior should therefore strongly weaken gravitational atmospheric tides, yielding a residual surface pressure amplitude of only ~ 5 Pa, with a phase shift of 5–20 h. Tidal winds are very weak, of the order of 3×10^{-4} m s^{-1} in the lower troposphere. Finally, constraints from Dragonfly data may permit the real and the imaginary parts of $k_2 - h_2$ to be estimated with a precision of ± 0.01–0.03.
Conclusions. Measurements of pressure variations by Dragonfly over the whole mission could give valuable constraints on the thickness of Titan's ice shell, and, via geophysical models, its heat flux and the density of its internal ocean.

Key words. planets and satellites: individual: Titan – planets and satellites: atmospheres – planets and satellites: interiors

1. Introduction

Just as Saturn's massive gravity causes tides both in Titan's interior as well as its surface seas, it causes a tide in the atmosphere (Lorenz 1992; Tokano & Neubauer 2002; Strobel 2006). Tokano & Neubauer (2002) analysed these gravitational atmospheric tides with a 3D global climate model (GCM). They found that the tidal potential produced by Saturn would generate a surface pressure variation of ~1.3 hPa through the orbit of Titan and tidal winds in the troposphere, with a mean wind speed of ~0.3–0.4 m s^{-1} at 300 m. Walterscheid & Schubert (2006) and Strobel (2006) studied these gravitational tidal waves with an analytical model. They found that tidal winds should increase with altitude until saturation in the upper atmosphere, where they would deposit energy. Walterscheid & Schubert (2006) suggested that the vertical transport by gravitational tides could produce the haze layers in Titan's upper atmosphere. However, these atmospheric studies did not take into account the deformation of Titan's interior. Titan likely possesses an internal water-rich ocean, as suggested from the elevated Love number $k_2 \sim 0.62$ measured by the spacecraft Cassini (Iess et al. 2012; Durante et al. 2019). Such a large induced gravitational potential implies a large deformation of the interior, which should strongly impact atmospheric tides. Measuring them could provide additional constraints on Titan's internal structure.

Dragonfly, a relocatable lander for Titan (Lorenz et al. 2018), is presently under development as part of NASA's fourth New Frontiers mission, with a view to launch in 2027 and arrive in 2034. Its objectives include assessing Titan's habitability, and thus probing Titan's internal structure. In this context, this paper indicates a new means by which Dragonfly may address this topic through measurements of pressure variations. In Sect. 2, we express the tidal potential exerted by Saturn on Titan's atmosphere, including the deformation of the interior. We reanalyse gravitational atmospheric tides with analytical calculations and with a 3D GCM in Sect. 3. Then, we discuss the possibility of constraining Titan's interior with Dragonfly in Sect. 4. We finish with a summary and conclusions in Sect. 5.

2. Computation of Saturn's tidal potential for Titan's atmosphere

2.1. Expression of Saturn's tidal potential

Titan orbits Saturn with a synchronous rotation rate. Its large orbital eccentricity ($e = 0.0292$) leads to time-dependent tides. Tides are due to both the time variation of the distance between Titan and Saturn (radial tide) and the time variation of Saturn's angular position from the sub-Saturnian point (librational tide). The tidal potential produced by Saturn can be expressed as

(Sagan & Dermott 1982; Tokano & Neubauer 2002)

$$V = -\frac{GM_S}{a}\left(\frac{R_T}{a}\right)^2 \left(\frac{3}{2}\cos^2(\lambda)\cos^2(\phi) - 1\right) - 3e\frac{GM_S}{a}\left(\frac{R_T}{a}\right)^2$$
$$\times \left[\frac{1}{2}(3\cos^2(\lambda)\cos^2(\phi) - 1)\cos(\Omega t) + \cos^2(\lambda)\sin(2\phi)\sin(\Omega t)\right],$$
(1)

where ϕ is the longitude from the sub-Saturnian point, λ is the latitude, $e = 0.0292$ is Titan's eccentricity around Saturn, $G = 6.673 \times 10^{-11}\,\mathrm{N\,m^2\,kg^{-2}}$ is the universal gravitational constant, $M_S = 5.685 \times 10^{26}$ kg is the mass of Saturn, $R_T = 2575$ km is Titan's radius, $a = 1.222 \times 10^9$ m is Titan's semi major axis, t is the time (measured from periapsis, when Titan is at the nearest point of Saturn), and $\Omega = 4.56 \times 10^{-6}\,\mathrm{rad\,s^{-1}}$ is Titan's orbital angular velocity.

The first term in Eq. (1) is time independent. This implies a permanent modification of Titan's geoid and interior with no impact on the atmospheric dynamics. We focus on the time-dependent terms of Eq. (1), which are related to Titan's eccentricity. The dynamic tidal potential can be expressed as

$$V_{dyn} = \frac{-V_0}{2}(3\cos^2(\lambda)\cos^2(\phi) - 1)\cos(\Omega t),$$
$$+ V_0\cos^2(\lambda)\sin(2\phi)\sin(\Omega t)$$
(2)

with

$$V_0 = -\frac{GM_S}{a}\left(\frac{R_T}{a}\right)^2 3\,e,$$
(3)

where $V_0 = -12.08\,\mathrm{m^2\,s^{-2}}$. We can express this potential as a superposition of prograde (eastward), retrograde (westward), and stationary waves:

$$V_{dyn} = -V_0\left[\frac{7}{8}\cos^2(\lambda)\cos(2\phi - \Omega t) - \frac{1}{8}\cos^2(\lambda)\cos(2\phi + \Omega t)\right]$$
$$+ V_0\left(\frac{3}{4}\cos^2(\lambda) - \frac{1}{2}\right)\cos(\Omega t)$$
(4)

or with normalised associated Legendre polynomials $P_{r,s}(\mu)$ and $\mu = \sin\lambda$:

$$V_{dyn} = -\frac{7}{6}\sqrt{\frac{3}{5}}V_0 P_{2,2}(\mu)\cos(2\phi - \Omega t)$$
$$+ \frac{1}{6}\sqrt{\frac{3}{5}}V_0 P_{2,2}(\mu)\cos(2\phi + \Omega t) - \frac{V_0}{\sqrt{10}}P_{2,0}(\mu)\cos(\Omega t).$$
(5)

The first term is a diurnal eastward wave (wave number = 2), the second term is a diurnal westward wave (wave number = 2) and the last term is a stationary wave. The eastward wave dominates at low latitudes, and the stationary wave dominates at high latitudes. We can also express the dynamic tidal potential (2) as

$$V_{dyn} = V_1\cos(\psi - \Omega t),$$
(6)

with $V_1 = -V_0\sqrt{\frac{1}{4}\left(3\cos^2(\lambda)\cos^2(\phi) - 1\right)^2 + \cos^4(\lambda)\sin^2(2\phi)}$

and $\psi = \arctan\left[\frac{2\cos^2(\lambda)\sin(2\phi)}{3\cos^2(\lambda)\cos^2(\phi) - 1}\right]$. This expression directly gives
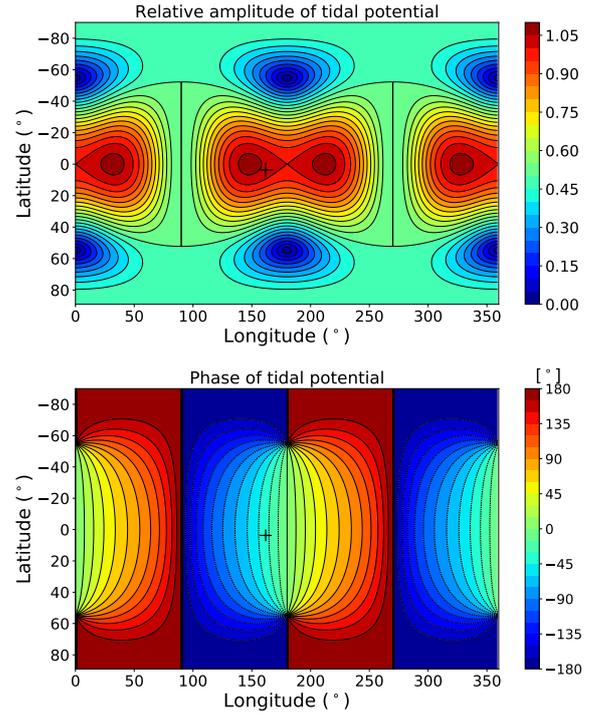
Fig. 1. Relative amplitude (V_1/V_0) and phase (ψ) of the dynamic tidal potential as a function of longitude and latitude. The black cross indicates Dragonfly's landing site.

the local wave amplitude as shown in Fig. 1. The tidal wave amplitude is maximal for $\lambda = 0°$ N and $\phi = \pm 32°$ (modulo 180°). It is null for $\lambda = \pm 60°$ N and $\phi = 0°/180°$. It is equal to V_0 at the sub-Saturnian and anti-Saturnian points.

Tyler (2008) pointed out the presence of obliquity tidal forces on a moon with a non-zero obliquity. In such a case, the obliquity tidal potential is given by

$$V_{obliquity} = \frac{3}{2}\Omega^2 R_T^2\theta_0\cos(\lambda)\sin(\lambda)\left(\cos(\phi - \Omega t) + \cos(\phi + \Omega t)\right),$$
(7)

where θ_0 is the obliquity in radians. $\theta_0 = 0.0052$ rad for Titan (0.3°). Using Kepler's third law ($\Omega^2 = \frac{GM_S}{a^3}$), the obliquity tidal potential can be expressed as

$$V_{obliquity} = -V_0\frac{\theta_0}{2e}\cos(\lambda)\sin(\lambda)\left(\cos(\phi - \Omega t) + \cos(\phi + \Omega t)\right). \quad (8)$$

The ratio of the amplitude of the obliquity tide by the amplitude of the eccentricity tide is approximately $\frac{\theta_0}{2e}\tan(\lambda)$. The obliquity tide dominates at latitudes higher than 80° on Titan. It is thus necessary to take into account the obliquity tide to study Titan's sea tides (see Tokano 2010a; Tokano et al. 2014; Vincent et al. 2016, 2018). In contrast, the eccentricity tide dominates at low latitudes. Its amplitude should be ~100 times that of the obliquity tide at Dragonfly's landing site (7° N 199° W). We therefore neglected the effect of the obliquity tide throughout this study, which focuses on Titan's equatorial regions.

2.2. Influence of the deformation of Titan's interior

The moment of inertia inferred from Cassini gravity measurements ($C/MR^2 \simeq 0.34$, Iess et al. 2010) indicates that Titan's

interior is differentiated into an outer hydrosphere and an inner rocky core (Castillo-Rogez & Lunine 2010; Sotin et al. 2021). The relatively high value of C/MR^2 suggests a low density and large rocky core (>2050–2100 km), potentially containing a significant fraction of organics (Néri et al. 2020). The determination of time variations of Titan's gravity field due to Saturn's tides by Cassini (Iess et al. 2012; Durante et al. 2019) provided clear evidence that Titan possess a liquid layer underneath its icy surface, most likely a water ocean (Mitri et al. 2014). The high value of the Love number, $k_2 = 0.616 \pm 0.067$, which quantifies the amplitude of induced-gravitational potential, suggested that the ocean is dense and salty (Mitri et al. 2014). However, as the uncertainties on k_2 are still large, the ocean depth and density remains unconstrained. Due to the high pressure reached at the bottom of the hydrosphere, high-pressure ice polymorphs (phase V and VI) are expected to form (e.g. Journaux et al. 2020). The thickness of this high-pressure layer is conditioned by the thickness of the outer ice shell and the composition of the ocean. For a thin outer layer (<50–70 km), it is possible that no high-pressure ice layer exists and that the ocean is in direct contact with the rocky core, which would strongly enhance the astrobiological potential of Titan's internal ocean. Constraining the outer ice shell thickness would therefore provide crucial constraints on the habitability of Titan.

The deformation of Titan's interior in response to Saturn's tides results in an change of the gravitational potential induced by time-varying internal mass redistribution, proportionally to the gravitational Love number k_2 mentioned above, together with a time-varying deflection of the surface that is proportional to the displacement Love number h_2. During high tides, k_2 results in an increase of tidal potential exerted on Titan's atmosphere and hence induced surface pressure, while h_2 results in a reduction due to surface elevation. If the interior behaves as a perfectly elastic body, the internal response would be in phase with the tidal potential produced by Saturn (Eq. (1)). In reality, Titan's interior is not perfectly elastic, part of the mechanical energy is dissipated in the interior and surface by various friction processes (Sohl et al. 1995; Tobie et al. 2005; Tokano et al. 2014; Lorenz et al. 2014). This results in an out-of-phase term whose amplitude depends on the mechanical properties of the interior. The in-phase term is represented by the real part of the Love number, whereas the out-of-phase term corresponds to the imaginary part. As a consequence, the tidal potential exerted on Titan's atmosphere can be expressed as

$$V_{\text{atm}} = V_1 \left[(1 + \Re(k_2 - h_2)) \cos(\Omega t - \psi) - \Im(k_2 - h_2) \sin(\Omega t - \psi) \right], \tag{9}$$

where k_2 and h_2 are the second-degree complex Love number. $\Re()$ and $\Im()$ are the real part of these complex numbers. The local amplitude of the tidal potential is thus reduced by a factor of $\gamma_2 = \sqrt{(1 + \Re(k_2 - h_2))^2 + \Im(k_2 - h_2)^2}$ (Sohl et al. 1995; Tokano et al. 2014; Lorenz et al. 2014) and has a phase shift of $\psi_2 = -\arctan\left(\frac{\Im(k_2 - h_2)}{1 + \Re(k_2 - h_2)}\right)$.

Pre-Cassini interior models predicted that γ_2 should be small, lower than 0.2, and probably lower than 0.1 (Sohl et al. 2003, e.g.). Here, we compute the complex Love numbers k_2 and h_2 following the approach used in Mitri et al. (2014), assuming a viscoelastic compressible interior (Tobie et al. 2005), and considering interior structure models reproducing the mean density (1881 kg/m3) and the reduced moment of inertia (0.341) of Titan. We considered interior structures consisting of four main layers from centre to surface: a rocky core, a high-pressure

(HP) ice V–VI layer, a liquid water ocean, and an ice I layer. The tidal response was computed using the formulation of the spheroidal deformation developed by Takeuchi & Saito (1972), initially derived for the elastic case, extended to the viscoelastic case by solving it in the frequency domain and by defining complex shear and bulk modulii, which is equivalent to the elastic modulii used in the elastic problem (see Tobie et al. 2005 for more details). For the liquid ocean layer, the simplified formulation of Saito (1974) was employed assuming a quasi-static and non-dissipative fluid material. To compute the viscoelastic deformation of the solid layers, we assumed a compressible Andrade model defined from bulk modulus, K, shear modulus, S, viscosity, η, and two empirical parameters α and β, which describe the transient response of the viscoelastic medium (Castillo-Rogez et al. 2011). Following Castillo-Rogez et al. (2011), we assumed the relationship $\beta \sim S^{-(1-\alpha)} \eta^{-\alpha}$ and chose a reference value of 0.25 for α. The rheological parameters were assumed constant in each internal layer, except in the outer ice layer where the viscosity, η, as a function of depth, was computed from a given temperature profile, which was either conductive or convective. In the conductive case, a temperature profile varying linearly from the surface to the bottom of the ice shell was considered. In the convective case, the ice shell is separated in a conductive lid and a convective isothermal sub-layer. The thickness of the conductive lid, b_{lid}, is determined from an imposed surface heat flux and the viscosity of the convective layer is determined from Nusselt-Rayleigh scaling laws (Dumoulin et al. 1999) in order to reproduce a convective heat flux equal to the imposed surface heat flux, ϕ_S, varying between 15 and 30 mW m^{-2} (see Appendix A in Lefevre et al. 2014 for more details). In the conductive part of the ice shell, the viscosity was computed from the linear temperature profile using an Arrhenius law:

$$\eta(z) = \eta_{T_b} \exp\left(\frac{E_a}{R(T(z) - T_b)}\right), \tag{10}$$

where T_b is the temperature at the bottom of the conductive shell, E_a is the activation energy ($E_a = 50$ kJ mol^{-1}), and R is the gas constant.

Figure 2 shows the computed values of $1 + \Re(k_2 - h_2)$, $\Im(k_2 - h_2)$, and $\Re(k_2)$ as functions of the ice shell thickness, the convective heat flux, and the ocean density. This figure suggests that accurate measurements of $1 + \Re(k_2 - h_2)$ and $\Im(k_2 - h_2)$ could constrain the ice shell thickness and the thermal state of the ice shell (conductive vs. convective) and could potentially give some estimate of the internal heat flux. For a conductive ice shell, $\Re(\gamma_2) = 1 + \Re(k_2 - h_2)$ is directly proportional to the ice shell thickness. For a convective ice shell, the relationship between $\Re(\gamma_2)$ and the ice shell thickness is less straightforward. However, by assessing both $\Re(\gamma_2)$ and $\Im(\gamma_2)$, the ice shell thickness and the vigor of convection can be determined unambiguously. Once the ice shell thickness has been constrained from γ_2 measurements, the measurements of $\Re(k_2)$ can be used to constrain the density of the ocean and hence its solute content.

As demonstrated in the next section, the gradient of surface pressure perfectly compensates the gradient of tidal potential, with almost no phase shift. The surface pressure variation is thus equal to $-\rho_0 V_{\text{atm}}$, where ρ_0 is the density of Titan's atmosphere at the surface. The deformation of the interior would therefore reduce the amplitude of the tidal pressure variations by γ_2, passing from ~64 Pa at the sub-Saturnian point, to likely less than 6.4 Pa for $\gamma_2 < 0.1$. Figure 3 shows the local amplitude of the tidal pressure variations ($\Delta P_{\text{surf}} = \gamma_2 \rho_0 V_1$) and phase compared to the sub-Saturnian point ($\psi + \psi_2$), without interior
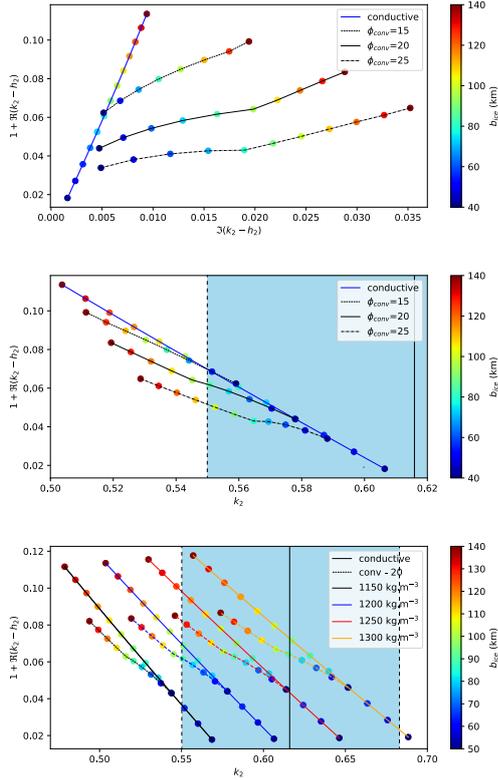
Fig. 2. Titan's values of $1 + \Re(k_2 - h_2)$, $\Im(k_2 - h_2)$, and $\Re(k_2)$ as functions of the ice shell thickness, the convective flux (given in mW m^{-2}), and the internal ocean density. The average ocean density was fixed at 1200 kg m^{-3} for the *top* and the *middle panels*. The blue area in the *middle* and *bottom panels* shows the values compatible with Cassini data at 1-sigma ($\Re(k_2) = 0.549$–0.683).

deformation (left), and with interior deformation (right), using $1 + \Re(k_2 - h_2) = 0.08$ and $\Im(k_2 - h_2) = 0.01$. These values correspond to an ice shell thickness of 80 km and a convective heat flux of 15 mW m^{-2}. We use these values as references in the rest of the paper. In this case, $\gamma_2 = 0.081$, $\psi_2 = -0.124$ rad (corresponding to a time shift or -7.6 h), and the amplitude of pressure variation at the sub-Saturnian point is equal to $\Delta P_{surf} = 5.2$ Pa.

3. Computation of atmospheric tides

3.1. Analytical solution

We derived the analytical solution of gravitational atmospheric tides caused by Saturn following the tidal theory from Chapman & Lindzen (1970) developed for the solar thermal tides and the lunar gravitational tides on Earth. This formalism was also used by Strobel (2006) to study the development of gravitational tidal waves in Titan's upper atmosphere. In Titan's troposphere, where winds are weak (geostrophic regime), gravitational atmospheric tides can be described by the following equations (the linearised primitive equations with no advective term), adding the gravitational tidal potential:

$$\frac{\partial u}{\partial t} - 2\Omega \sin(\lambda) v = -\frac{1}{R_T \cos(\lambda)} \frac{\partial(\Phi + V_{atm})}{\partial \phi}$$
$$\frac{\partial v}{\partial t} + 2\Omega \sin \lambda\, u = -\frac{1}{R_T} \frac{\partial(\Phi + V_{atm})}{\partial \lambda}$$
$$\frac{1}{R_T \cos \lambda}\left(\frac{\partial u}{\partial \phi} + \frac{\partial v \cos \lambda}{\partial \lambda}\right) + \frac{1}{\rho_0} \frac{\partial \rho_0 w}{\partial z} = 0 \qquad (11)$$
$$\frac{\partial^2 \Phi}{\partial z \partial t} + N^2 w = 0,$$

where u, v, and w are the zonal, meridional, and vertical winds; ρ_0 is the air density; Φ is the geopotential; and p is the pressure. $N = \sqrt{\frac{g}{\theta} \frac{d\theta}{dz}} = \sqrt{\frac{g}{T}(\Gamma_d - \Gamma)}$ is the Brunt-Väisälä frequency (θ is the potential temperature and Γ and Γ_d are the temperature gradient and the adiabatic temperature gradient of the atmosphere). $N \sim 0.001$ s^{-1} in the first 2 km of Titan's troposphere (Charnay & Lebonnois 2012). The atmosphere is forced by a tidal potential periodic in longitude and time. We searched complex solutions of the following form:

$$(u, v, w, \Phi, V_{atm}) = Re[(\hat{u}, \hat{v}, \hat{w}, \hat{\Phi}, \hat{V}_{atm})e^{i(s\phi + 2\Omega\sigma t)}], \qquad (12)$$

with $\sigma = 1$ and $s = -1/2$ for the eastward mode, $\sigma = 1$ and $s = 1/2$ for the westward mode, and $\sigma = 1$ and $s = 0$ for the stationary mode. Solutions satisfy the following equations:

$$\hat{u} = \frac{-\sigma}{2a\Omega} S_u^{\sigma,s}(\hat{\Phi} + \hat{V}_{atm})$$
$$\hat{v} = \frac{i\sigma}{2a\Omega} S_v^{\sigma,s}(\hat{\Phi} + \hat{V}_{atm})$$
$$\mathcal{L}^{\sigma,s}\hat{\Phi} - i\frac{2R_T^2\Omega}{\sigma\rho_0}\frac{\partial(\rho_0\hat{w})}{\partial z} = -\mathcal{L}^{\sigma,s}\hat{V}_{atm} \qquad (13)$$
$$2i\Omega\sigma\frac{\partial\hat{\Phi}}{\partial z} + N^2\hat{w} = 0,$$

where $\mathcal{L}^{\sigma,s}$ is the Laplace tidal operator given by

$$\mathcal{L}^{\sigma,s}\hat{\Phi} = \partial_\mu\left(\frac{1 - \mu^2}{\sigma^2 - \mu^2}\partial_\mu\hat{\Phi}\right) - \frac{1}{\sigma^2 - \mu^2}\left(\frac{s(\sigma^2 + \mu^2)}{\sigma(\sigma^2 - \mu^2)} + \frac{s^2}{1 - \mu^2}\right)\hat{\Phi}. \qquad (14)$$

$S_u^{\sigma,s}$ and $S_u^{\sigma,s}$ are the horizontal wind operators given by

$$S_u^{\sigma,s} = \left[\frac{s}{\sigma^2 - \mu^2} - \frac{\mu(1 - \mu^2)}{\sigma(\sigma^2 - \mu^2)}\frac{\partial}{\partial\mu}\right]$$
$$S_v^{\sigma,s} = \left[\frac{s}{\sigma(\sigma^2 - \mu^2)} - \frac{(1 - \mu^2)}{(\sigma^2 - \mu^2)}\frac{\partial}{\partial\mu}\right], \qquad (15)$$

with $\mu = \sin \lambda$. Eigenvectors of the Laplace tidal operator are the Hough functions $\Theta_n^{\sigma,s}$, which verify

$$\mathcal{L}^{\sigma,s}\Theta_n^{\sigma,s} + \gamma_n^{\sigma,s}\Theta_n^{\sigma,s} = 0. \qquad (16)$$

The eigenvalues $\gamma_n^{\sigma,s}$ are called the Lamb parameters, which are also defined with equivalent heights $h_n^{\sigma,s}$ with $\gamma_n^{\sigma,s} = 4\Omega^2 R_T^2/(gh_n^{\sigma,s})$.

If we decompose the tidal potential and solutions in terms of Hough functions, $\hat{V}_{atm} = \sum_{n=1}^{\infty} V_n^{\sigma,s}\Theta_n^{\sigma,s}$ and $(\hat{u}, \hat{v}, \hat{w}, \hat{\Phi}) = \sum_{n=1}^{\infty}(\hat{u}_n, \hat{v}_n, \hat{w}_n, \hat{\Phi}_n)\Theta_n^{\sigma,s}e^{z/2H}$, the problem is reduced to the resolution of an equation on the vertical structure:

$$\frac{d^2\hat{w}_n}{dz^2} + \left(\frac{N^2}{gh_n^{\sigma,s}} - \frac{1}{4H^2}\right)\hat{w}_n = 0, \qquad (17)$$

with $\frac{D\Phi}{Dt} = 0$ as the boundary condition at the surface, which can be expressed as

$$\frac{d\hat{w}_n}{dz} + \left(\frac{1}{h_n^{\sigma,s}} - \frac{1}{2H}\right)\hat{w}_n = \frac{2i\sigma\Omega V_n^{\sigma,s}}{gh_n^{\sigma,s}}. \qquad (18)$$

To compute the pressure and wind variations analytically, we first computed the Hough functions and Lamb parameters for given values of σ and s using the algorithm from
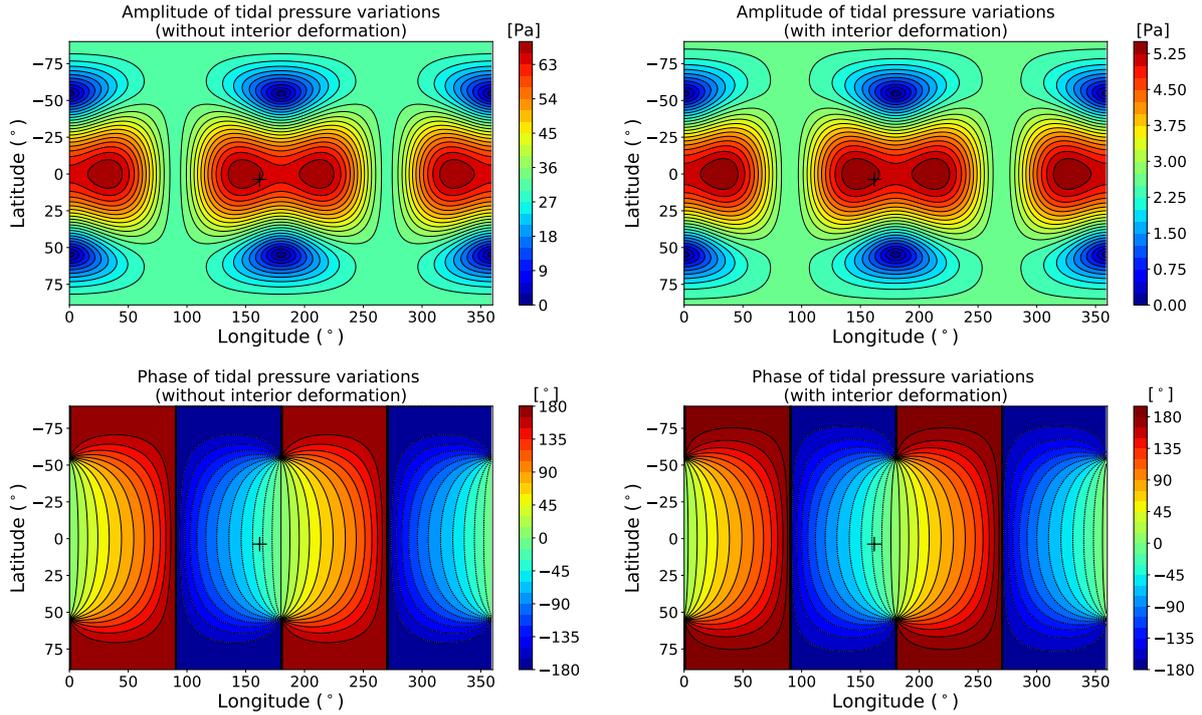
Fig. 3. Amplitude of tidal pressure variations (*top panel*) and phase (*bottom panel*) as a function of longitude and latitude, without interior deformation (*left*) and with interior deformation (*right*). The latter is computed with $1+\Re(k_2 - h_2) = 0.08$ and $\Im(k_2 - h_2) = 0.01$. The black cross indicates Dragonfly's landing site.

Wang et al. (2016). Then, we expanded the tidal potential in Hough functions. We solved the vertical structure equation for each mode n, assuming an upward wave propagation for $(\frac{1}{h_n^{\sigma,s}} - \frac{1}{2H}) \geq 0$ and an evanescent wave for $(\frac{1}{h_n^{\sigma,s}} - \frac{1}{2H}) < 0$. Since $h_n^{\sigma,s} \ll H$ for all modes, the wave propagation only depends on the sign of $h_n^{\sigma,s}$. Then, we solved the surface boundary condition and we determined $\hat{u}_n$, $\hat{v}_n$, $\hat{w}_n$, and $\hat{\phi}_n$ in complex form. Finally, we summed results over n to obtain the pressure and wind fields. Figure 4 shows the amplitude of the surface pressure variation for the eastward and westward tidal waves. The surface pressure perfectly follows the tidal forcing for both cases. Figure 5 shows maps of tidal surface pressure and winds at a given time for the eastward and westward modes. The maximal tidal wind speed is 3×10^{-4} m s^{-1}, which is three orders of magnitude lower than the typical surface wind speed predicted by 3D GCMs (e.g. Lebonnois et al. 2012; Charnay & Lebonnois 2012).

3.2. Simulations with the Titan IPSL GCM

We performed 3D simulation with the Titan IPSL GCM (Lebonnois et al. 2012) including the tidal potential caused by Saturn. We used a horizontal resolution of 32×48 (corresponding to resolutions of 11.25° longitude by 3.75° latitude) and 55 vertical levels. Simulations were run for ten Titan days at the vernal equinox with thermal tides and with and without gravitational tides. Dragonfly will operate during the southern summer, but we did not notice influence of the season on the amplitude of gravitational tides. We used the tidal potential without or with interior deformation (with $1 + \Re(k_2 - h_2) = 0.08$ and $\Im(k_2 - h_2) = 0.01$). We analysed simulations from day 5 to day 10, removing the first five days during which the atmosphere readjusts to the presence or absence of tides.
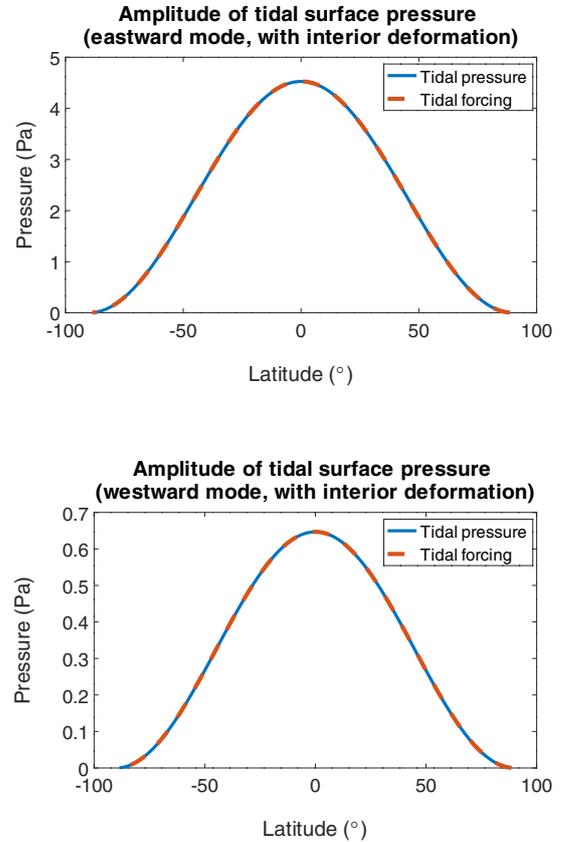

Fig. 4. Amplitude of atmospheric surface pressure for the eastward (*top*) and westward (*bottom*) tidal wave compared to the tidal forcing. Analytical calculation including interior deformation with $1 + \Re(k_2 - h_2) = 0.08$ and $\Im(k_2 - h_2) = 0.01$.
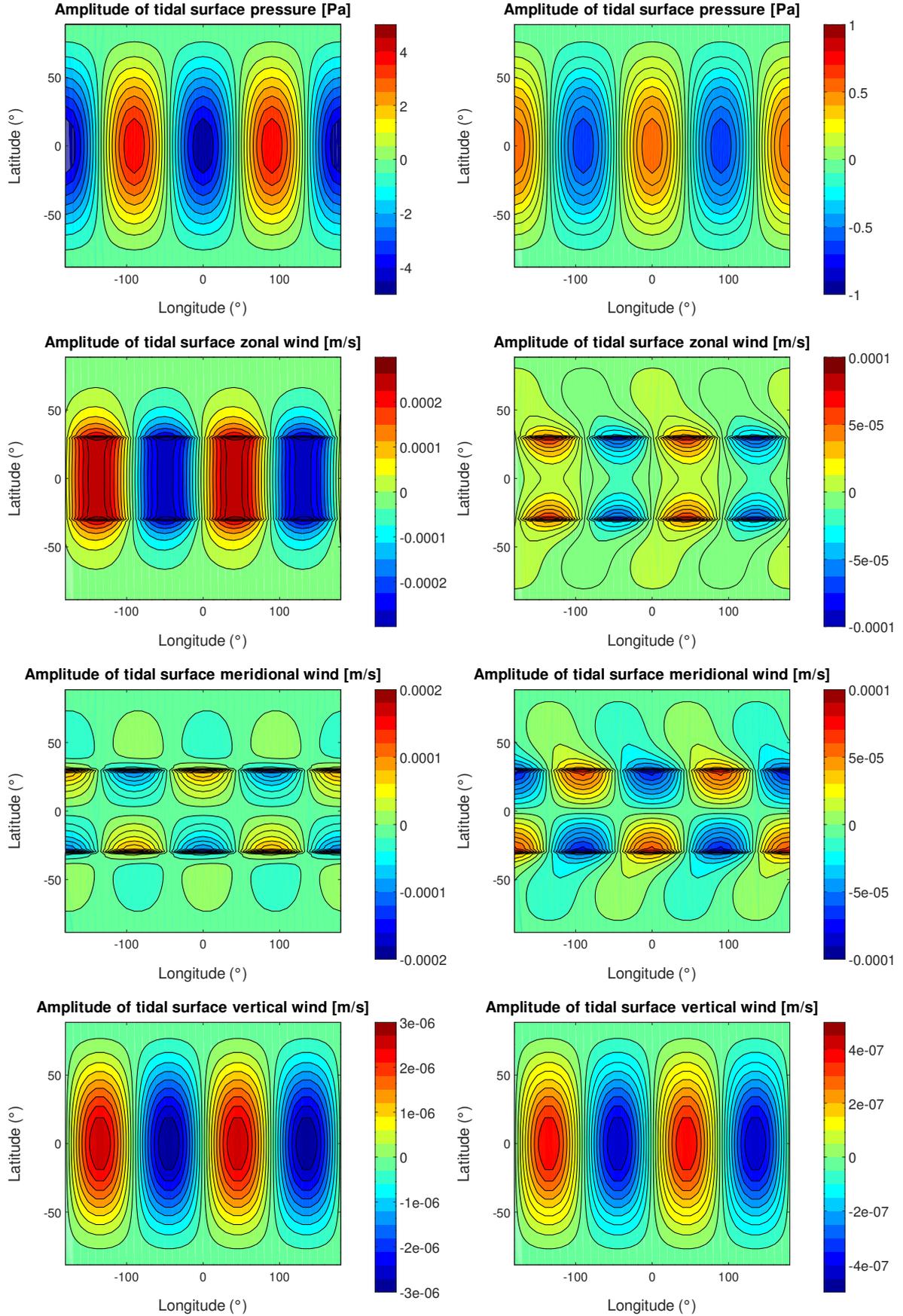
Amplitude of tidal surface pressure [Pa]

Amplitude of tidal surface pressure [Pa]

Amplitude of tidal surface zonal wind [m/s]

Amplitude of tidal surface zonal wind [m/s]

Amplitude of tidal surface meridional wind [m/s]

Amplitude of tidal surface meridional wind [m/s]

Amplitude of tidal surface vertical wind [m/s]

Amplitude of tidal surface vertical wind [m/s]

Fig. 5. Tidal surface pressure and tidal zonal, meridional, and vertical surface winds as functions of longitude and latitude at $t = 0$ for the eastward wave (*left*) and the westward wave (*right*). Analytical calculation including interior deformation with $1 + \Re(k_2 - h_2) = 0.08$ and $\Im(k_2 - h_2) = 0.01$.
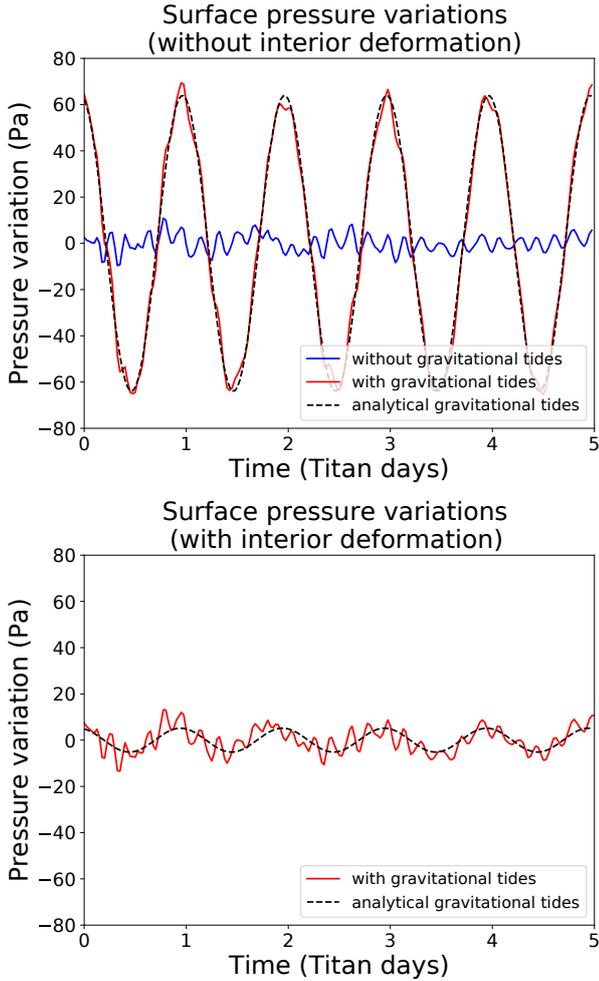
Fig. 6. Pressure variations at longitude 0° and latitude 0°N computed with the Titan IPSL GCM. The *top* (*bottom*) panel shows the effects of gravitational tides without (with) interior deformation. The case with interior deformation assumed $1 + \Re(k_2 - h_2) = 0.08$ and $\Im(k_2 - h_2) = 0.01$. Thermal tides were included in all simulations. The blue line in the *top panel* shows the pressure variations without gravitational tides for comparison. The analytical tidal pressure variation is shown with a black dashed line.

Simulated pressure and horizontal wind variations confirm the analytical calculations from the previous sub-section. The pressure field follows the tidal potential, and tidal winds are very weak in the simulations. Figure 6 shows the time evolution of the surface pressure at the sub-Saturnian point (longitude 0° and latitude 0°) with thermal tides (diurnal solar cycle) and with/without gravitational tides. For the case without interior deformation (left panel), the gravitational tides dominate the surface pressure variations that follow the tidal potential well. The standard deviation of the surface pressure without gravitational tides or subtracting the theoretical tidal pressure is around 4 Pa. This is less than the amplitude of the tidal pressure variations for the case with interior deformation (i.e. $\Delta P = 5.2$ Pa). Although small, the tidal signal is clearly identified in the simulation with interior deformation (right panel).

We found that the gravitational tides have a negligible effect on the surface temperature (variations of $\sim 10^{-3}$ K correlated with surface pressure for the case with deformation of the interior), which is dominated by the diurnal solar cycle (peak-to-peak variations of ~ 0.5 K). Figure 7 shows the surface pressure
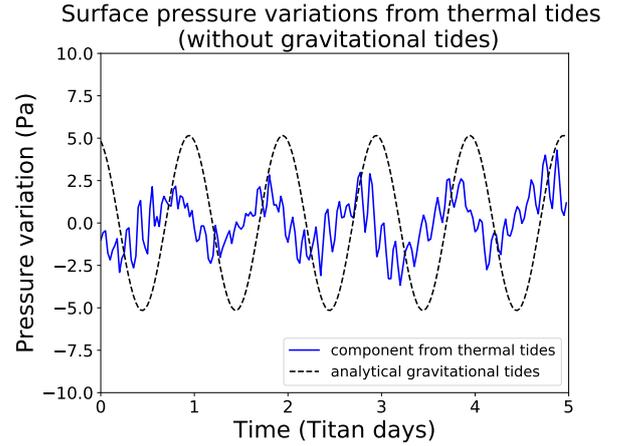

Fig. 7. Pressure variations caused by thermal tides at longitude 0° and latitude 0°N computed with the Titan IPSL GCM. The analytical pressure variation from gravitational tides with interior deformation is shown with a black dashed line.

variations from thermal tides for the case without gravitational tides. It was computed by making the direct subtraction of a simulation with thermal tides minus without thermal tides. It reveals that the surface pressure variations from thermal tides are dominated by the diurnal mode, as also found by Tokano (2010b). It has an amplitude of 1.7 Pa, smaller than gravitational tides and with a phase shift (the maximum occurs at ~ 6 pm solar local time). In contrast, the pressure variation from thermal tides on Earth are dominated by the semi-diurnal mode (Chapman & Lindzen 1970). It is forced in particular by the solar energy absorption by stratospheric ozone and has two pressure maximums at ~ 10 a.m. and ~ 10 p.m. solar local time.

In our simulations, a major source of variability in the lower troposphere comes from baroclinic waves, which develop at mid-latitudes with a period of 2–5 Titan days and a pressure variation of ~ 20 Pa (Lebonnois et al. 2012). However, their impact is limited in the equatorial region (pressure variation of ~ 1 Pa), and they can be distinguished from gravitational tides by their long period. Mitchell et al. (2011) also found that equatorially trapped Kelvin waves with a period of ~ 0.5 Titan day would occur. They are likely responsible for the large chevron-shaped methane storm observed at the equator during the equinoctial season (Turtle et al. 2011). We did not identify these modes in our simulations. The variability caused by planetary waves in the equatorial region may thus be higher than predicted by our model, in particular close to the equinox when equatorial clouds and storms form.

Figure 8 shows the zonal tidal wind component at 35 m above the surface for the case with interior deformation. It was computed without thermal tides to eliminate their effect and by making the direct subtraction of a simulation with gravitational tides minus without gravitational tides. From day 5 to day 10, the wind field is sufficiently close between the two simulations (with and without gravitational tides) that the difference of surface wind corresponds quite well to the tidal component. The simulated tidal wind component is extremely weak, with an amplitude of $\sim 3 \times 10^{-4}$ m s^{-1} at the sub-Saturnian point. This is much lower than typical surface winds, which are around 0.5 m s^{-1} in the IPSL GCM (Lebonnois et al. 2012; Charnay & Lebonnois 2012). This tidal wind speed is consistent with our analytical calculations (see Sect. 2.2). Friedson et al. (2009) performed 3D simulations of Titan's atmosphere including gravitational tides
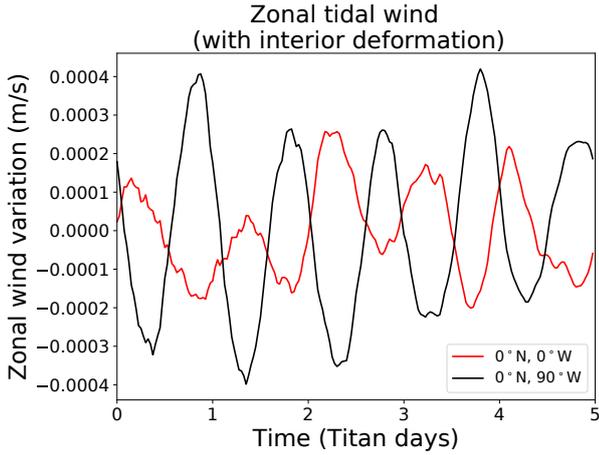
Fig. 8. Component of zonal tidal winds at 35 m above the surface computed at latitude 0°N and longitude 0°W (red) or 90°W (black). The lines correspond to the difference between simulations with tides and without tides. Thermal tides were not included in these simulations.

with the Titan-CAM model. They found an amplitude of tidal winds of around 0.05 m/s compared to 0.5 m/s in the simulations from Tokano & Neubauer (2002). Our simulated tidal winds are, respectively, two orders of magnitude and three orders of magnitude lower than those in the simulations from Friedson et al. (2009) and Tokano & Neubauer (2002). The deformation of the interior is responsible for a reduction of tidal wind speed by one order of magnitude, meaning that large discrepancies remain between the tidal responses of GCMs for the same forcing. These discrepancies could be related to the mean circulation or to the thermal structure. In particular, the tidal wind amplitude is proportional to N^2 (the squared Brunt-Väisälä frequency) and thus very sensitive to the thermal structure. The lower troposphere may be more adiabatic in the IPSL GCM than in the models by Tokano & Neubauer (2002) and Friedson et al. (2009), leading to weaker tidal winds. In this regard, the Titan IPSL GCM reproduces the thermal structure and the zonal wind measured by the Huygens probe in Titan's troposphere well, especially in the planetary boundary layer (Lebonnois et al. 2012; Charnay & Lebonnois 2012), giving us confidence in our predictions. According to our analytical and numerical calculations, tidal winds should not be detectable in Titan's lower troposphere.

3.3. Impact of tides on cloud formation

The tidal pressure variation and the associated adiabatic heating and warming induce a change of relative humidity, which can impact cloud formation and precipitation. A statistical analysis of 15 yr of data from ERA-Interim shows that the lunar semi-diurnal tide induces a variation of relative humidity and precipitation on Earth with amplitudes of 0.039% and 0.4%, respectively (Kohyama & Wallace 2016). One may wonder if the stronger Saturnian gravitational tides could affect cloud formation on Titan, with a preferential formation where the amplitude of tides are maximal (i.e. close to the sub-Saturnian and anti-Saturnian point). This mechanism has been suggested to explain the two maximums of cloud occurrence from Cassini close to longitudes 0°E and 180°E (Rodriguez et al. 2009).

The passage of the tidal wave is associated with an adiabatic warming or cooling:

$$dT = -\frac{R^*T}{c_pP}dP, \tag{19}$$

with R^* being the specific gas constant, c_p the specific heat capacity of Titan's atmosphere, T the temperature, and P the pressure. Above the surface, the amplitude of temperature variations caused by tides is $\sim 1 \times 10^{-3}$ K. The relative humidity of methane clouds defined as $RH = \frac{P_{vap}}{P_{sat}}$ evolves as

$$\frac{dRH}{RH} = \frac{dP_{vap}}{P_{vap}} - \frac{dP_{sat}}{P_{sat}}. \tag{20}$$

If we assume no condensation, $\frac{dP_{vap}}{P_{vap}} = \frac{dP}{P}$. The Clausius–Clapeyron relation gives $\frac{dP_{sat}}{dT} = \frac{L_{CH_4}P_{sat}}{R_{CH_4}T^2}$, where L_{CH_4} is the mass-latent heat of methane and R_{CH_4} is the specific gas constant of methane. These relations lead to

$$\frac{dRH}{RH} = \frac{dP}{P}\left(1 - \frac{L_{CH_4}R^*}{C_pR_{CH_4}T}\right). \tag{21}$$

For Titan's tropospheric conditions, $\frac{L_{CH_4}R^*}{C_pR_{CH_4}T} \sim 3.1$. The relative humidity is maximal when the tidal pressure is minimal. The maximal amplitude of relative humidity variation is around 0.01%. The effect is therefore very small, even four times smaller than the lunar tides on the Earth. We conclude that the influence of gravitational tides on Titan's clouds should not be detectable in Cassini data. Longitudinal variations of the cloud occurrence rate should instead be due to variations of surface properties (topography, surface humidity, albedo, or thermal inertia).

4. Implications for the Dragonfly mission

4.1. Dragonfly's ability to measure atmospheric tides

The Dragonfly mission is discussed in Turtle et al. (2018), Barnes et al. (2021), and Lorenz et al. (2018). In addition to the pressure or tide determination approach in the present paper, Dragonfly may also constrain the thickness of Titan's ice shell via the Schumann resonance (Lorenz & Le Gall 2020) and with seismic methods (Lorenz et al. 2019). We note that Dragonfly (now planned to launch in 2027) is still in an early design phase, and some of the following details may evolve. The Dragonfly initial landing site (Lorenz et al. 2021) is just south of the Selk crater at 7° N 199°W. This is fortunately rather close to the anti-Saturnian point, where the pressure tide amplitude is nearly at its maximum value (see Fig. 1).

The pressure measurement on Dragonfly Geophysics and Meteorology (DraGMet) package was specified in order to measure the boundary layer profile during flights up to 3 or 4 km. The absolute accuracy specification is therefore only about 2 mbar (200 Pa). However, the sensitivity to changes will be considerably better, and the telemetered resolution may be as good as 1 Pa. The precision that can be practically achieved (and thus the ability to detect small changes) will, as on other missions, be contingent on sensor noise performance and will likely be period dependent and lander activity dependent: tests in Phase A with representative sensors suggest that the ability to detect variations with an amplitude of 5 Pa on a range of periods should be possible with suitable filtering. As discussed in Chapman & Lindzen (1970), periodic changes can be detected in long-time-series data by virtue of averaging over many cycles. The Dragonfly nominal mission is 3 yr, or about 70 Tsols (Titan solar days). Crudely, diurnal signals may be measurable with a precision of $\sim 70^{0.5} \sim 8 \times$ better than that of individual measurements, offering good prospects that an atmospheric tidal

signal can be measured with a precision that can discriminate interior structure models. For comparison, the pressure sensor on the Huygens probe had an accuracy lower than 100 Pa and a resolution lower 1 Pa, quite similar to Dragonfly's sensors. The Huygens probe measured surface pressure on Titan for around 30 min (Harri et al. 2006). The standard deviation of those pressure readings was ~1 Pa, indicating that any variation in background pressure must have been slower than 2 Pa h^{-1}. Unfortunately, the measurement was not long enough to constrain the tides. The maximal pressure variation (for the ideal case with no deformation of the interior) due to tides at the Huygens site is $\frac{dP}{dt} = -\Omega\rho_0 V_0 \sim 1$ Pa h^{-1}. However, the precision of Huygen's measurements holds promise for Dragonfly's ability to detect tides.

It is probable that the largest confounding factor in retrieving a tidal pressure signal is that lander activities will be correlated with the time of (solar) day. Notably, rotorcraft flight and communication with Earth, both of which will entail appreciable energy dissipation in the lander; thus, some change in internal temperatures including the pressure sensor will occur during the daytime. Therefore, any analysis of the sort described here must be vigilant towards imperfections in the temperature compensation of the pressure measurement (a known challenge on other missions – e.g. Taylor et al. 2010), which may lead to a spurious signal with a period of one Tsol (i.e. the same period as the atmospheric tide), and it is likely that the magnitude of such effects will not be reliably known until arrival on Titan. Over three years of landed operations, however (a tenth of a Saturnian year), the phasing of the gravitational tidal peak, fixed with respect to Titan's orbit around Saturn and thus in inertial space, will change with respect to local solar time (due to the difference in length of the solar and sidereal day), which will mitigate this problem. It should also be recognised that while DraGMet is intended to measure pressure data many times per Titan day (perhaps Earth-hourly, with some bursts of higher-rate data), the record will have step-like jumps in pressure owing to the different elevations of various landing sites. Thus, some manual editing and adjustment preprocessing of the time series may be necessary to most precisely extract a tidal signal.

4.2. Constraints on Titan's interior

As discussed in Sect. 2, the second-degree Love numbers (k_2 and h_2) and the surface pressure variations are related by

$$P_{\mathrm{surf}} = -\rho_0 V_1 (1 + \Re(k_2 - h_2)) \cos(\Omega t - \psi) \\ + \rho_0 V_1 \Im(k_2 - h_2) \sin(\Omega t - \psi) . \tag{22}$$

Assuming that Dragonfly's pressure measurements have a Gaussian noise with an uncertainty equal to σ_P, the uncertainty on the tidal pressure amplitude would be equal to $\sqrt{\frac{2}{N_{\mathrm{obs}}}}\sigma_P$ and the uncertainty on $1 + \Re(k_2 - h_2)$ and $\Im(k_2 - h_2)$ would be equal to $\sqrt{\frac{2}{N_{\mathrm{obs}}}}\frac{\sigma_P}{\rho_0 V_1}$, where N_{obs} is the number of measurements (Alegria & Serra 2006). Table 1 shows the uncertainty for these parameters after 1 or 70 Titan days, assuming a precision of either 50 Pa (optimistic case) or 200 Pa (pessimistic case) for each individual measurement, which was taken every hour (383 measurements per Tsol). The pessimistic case corresponds to the absolute accuracy specification. We chose a four-times-better precision for the optimistic case, able to detect a variation of 4 Pa amplitude after one Tsol. This is fairly consistent with initial tests of Dragonfly's pressure sensors. Based on these two scenarios, we expect that Dragonfly could detect tidal pressure variations

Table 1. Expected precision of Dragonfly measurements for the amplitude of tidal pressure variations, for the real and the imaginary parts of $k_2 - h_2$.

Case	Optimistic		Pessimistic	
Number of Tsols	1	70	1	70
Amplitude (Pa)	±4	±0.4	±14	±1.7
$\Re(h_2 - k_2)$	±0.06	±0.007	±0.2	±0.03
$\Im(h_2 - k_2)$	±0.06	±0.007	±0.2	±0.03

Notes. Values are computed for an optimistic case (precision of 50 Pa for each individual measurement) and a pessimistic case (precision of 200 Pa for each individual measurement). They are given for 1 Titan day or 70 Titan days (i.e. the whole mission), assuming measurements every hour (383 measurements per Titan day).

and could measure the real and imaginary parts of $(k_2 - h_2)$ with a precision of ±0.01–0.03 over the whole mission. This precision is comparable to the precision on k_2 from Cassini flybys and will be complementary to the k_2 estimate. According to Fig. 2, such values would allow us to derive the ice shell thickness with a precision of around ±15 km and to estimate the heat flux with a precision of around ±5 mW m^{-2} using interior models. Unfortunately, the determination of the ocean density would be limited by the precision on k_2. Some values of density could, however, be excluded. For instance $1 + \Re(k_2 - h_2) \geq 0.08$ would imply a density higher than 1250 kg m^{-3}.

5. Summary and conclusions

In this article, we reanalysed Titan's gravitational atmospheric tides, including the effects of the deformation of the interior. We showed that the tidal response of the interior, characterised by low values of $1 + \Re(k_2 - h_2)$ and $\Im(k_2 - h_2)$, should strongly decrease the tidal potential affecting the atmosphere. Using analytical calculations and 3D GCM simulations, we showed that the atmosphere should quickly respond to the tidal potential, with almost no phase shift and extremely weak tidal winds. We predict that the amplitude of the pressure variation should be ~5 Pa. This low value mitigates the possible effect of gravitational tides for transporting energy in the upper atmosphere, as suggested by Strobel (2006). In addition, the impact of gravitational tides on cloud formation should be totally negligible. Yet, the tidal pressure variations could be higher than the variations caused by thermal tides or planetary waves in the equatorial region. The methane cycle (i.e. tropospheric cloud formation and precipitation), which was not included in our 3D simulations, could be an additional source of variability.

Finally, we predict that Dragonfly can certainly detect the pressure signal that would be present if tidal deformation of the interior did not occur. It may even detect the small residual tidal pressure variations taking interior or crustal deformation into account. The real and imaginary part of $(k_2 - h_2)$ could then be inferred with a precision of ±0.01–0.03 over the whole mission, constraining the thickness of the ice shell and (via models) the internal heat flux with a precision of ~±15 km and ~±5 mW m^{-2}, respectively. These measurements are insensitive to the ocean density, but they can restrict the range of possible ocean density in combination with current k_2 estimate. A future orbiter around Titan could strongly improve the estimate of k_2. Combined with Dragonfly measurements, it could then constrain the density of the internal ocean, with implications on its composition, evolution, and habitability.

References

Alegria, F. C., & Serra, A. C. 2006, in 2006 IEEE Instrumentation and Measurement Technology Conference Proceedings, 1643

Barnes, J. W., Turtle, E. P., Trainer, M. G., et al. 2021, Planet. Sc. J., 2, 130

Castillo-Rogez, J. C., & Lunine, J. I. 2010, Geophys. Res. Lett., 37

Castillo-Rogez, J. C., Efroimsky, M., & Lainey, V. 2011, J. Geophys. Res.: Planets, 116

Chapman, S., & Lindzen, R. 1970, Atmospheric Tides (Dordrecht, HollandD: Reidel Publ. Co.), 200

Charnay, B., & Lebonnois, S. 2012, Nat. Geosci., 5, 106

Dumoulin, C., Doin, M.-P., & Fleitout, L. 1999, J. Geophys. Res.: Solid Earth, 104, 12759

Durante, D., Hemingway, D. J., Racioppa, P., Iess, L., & Stevenson, D. J. 2019, Icarus, 326, 123

Friedson, A. J., West, R. A., Wilson, E. H., Oyafuso, F., & Orton, G. S. 2009, Planet. Space Sci., 57, 1931

Harri, A.-M., Mäkinen, T., Lehto, A., Kahanpää, H., & Siili, T. 2006, Planet. Space Sci., 54, 1117

Iess, L., Rappaport, N. J., Jacobson, R. A., et al. 2010, Science, 327, 1367

Iess, L., Jacobson, R. A., Ducci, M., et al. 2012, Science, 337, 457

Journaux, B., Kalousová, K., Sotin, C., et al. 2020, Space Sci. Rev., 216, 1

Kohyama, T., & Wallace, J. M. 2016, Geophys. Res. Lett., 43, 918

Lebonnois, S., Burgalat, J., Rannou, P., & Charnay, B. 2012, Icarus, 218, 707

Lefevre, A., Tobie, G., Choblet, G., & Čadek, O. 2014, Icarus, 237, 16

Lorenz, R. D. 1992, in Proceedings of the Symposium on Titan, Toulouse, September 1991, 119

Lorenz, R. D., & Le Gall, A. 2020, Icarus, 351, 113942

Lorenz, R. D., Kirk, R. L., Hayes, A. G., et al. 2014, Icarus, 237, 9

Lorenz, R. D., Turtle, E. P., Barnes, J. W., et al. 2018, Johns Hopkins APL Technical Digest

Lorenz, R., Panning, M., Stahler, S., et al. 2019, Lunar Planet. Sci. Conf., 50, 2173

Lorenz, R. D., MacKenzie, S. M., Neish, C. D., et al. 2021, Planet. Sci. J., 2, 24

Mitchell, J. L., Ádámkovics, M., Caballero, R., & Turtle, E. P. 2011, Nat. Geosci., 4, 589

Mitri, G., Meriggiola, R., Hayes, A., et al. 2014, Icarus, 236, 169

Néri, A., Guyot, F., Reynard, B., & Sotin, C. 2020, Earth Planet. Sci. Lett., 530, 115920

Rodriguez, S., Le Mouélic, S., Rannou, P., et al. 2009, Nature, 459, 678

Sagan, C., & Dermott, S. F. 1982, Nature, 300, 731

Saito, M. 1974, J. Phys. Earth, 22, 123

Sohl, F., Sears, W. D., & Lorenz, R. D. 1995, Icarus, 115, 278

Sohl, F., Hussmann, H., Schwentker, B., Spohn, T., & Lorenz, R. D. 2003, J. Geophys. Res. (Planets), 108, 5130

Sotin, C., Kalousová, K., & Tobie, G. 2021, Annu. Rev. Earth Planet. Sci., 49, 579

Strobel, D. F. 2006, Icarus, 182, 251

Takeuchi, H., & Saito, M. 1972, in Methods in Computational Physics: Advances in Research and Applications, 11, Seismology: Surface Waves and Earth Oscillations, ed. B. A. Bolt (Elsevier), 217

Taylor, P. A., Kahanpää, H., Weng, W., et al. 2010, J. Geophys. Res. (Planets), 115, E00E15

Tobie, G., Mocquet, A., & Sotin, C. 2005, Icarus, 177, 534

Tokano, T. 2010a, Ocean Dyn., 60, 803

Tokano, T. 2010b, Planet. Space Sci., 58, 814

Tokano, T., & Neubauer, F. M. 2002, Icarus, 158, 499

Tokano, T., Lorenz, R. D., & Van Hoolst, T. 2014, Icarus, 242, 188

Turtle, E. P., Del Genio, A. D., Barbara, J. M., et al. 2011, Geophys. Res. Lett., 38, L03203

Turtle, E. P., Barnes, J., Trainer, M., et al. 2018, in Lunar Planet. Sci. Conf., 49

Tyler, R. H. 2008, Nature, 456, 770

Vincent, D., Karatekin, Ö., Vallaeys, V., et al. 2016, Ocean Dyn., 66, 461

Vincent, D., Karatekin, Ö., Lambrechts, J., et al. 2018, Icarus, 310, 105

Walterscheid, R. L., & Schubert, G. 2006, Icarus, 183, 471

Wang, H., Boyd, J. P., & Akmaev, R. A. 2016, Geosci. Model Dev., 9, 1477